Chemical and physical transformations of carbon-based nanomaterials observed by liquid phase transmission electron microscopy

Lucas R. Parent, Maria Vratsanos, Biao Jin, James J. De Yoreo, and Nathan C. Gianneschi

This article addresses recent advances in liquid phase transmission electron microscopy (LPTEM) for studying nanoscale synthetic processes of carbon-based materials that are independent of the electron beam—those driven by nonradiolytic chemical or thermal reactions. In particular, we focus on chemical/physical formations and the assembly of nanostructures composed of organic monomers/polymers, peptides/DNA, and biominerals. The synthesis of carbon-based nanomaterials generally only occurs at specific conditions, which cannot be mimicked by aqueous solution radiolysis. Carbon-based structures themselves are also acutely sensitive to the damaging effects of the irradiating beam, which make studying their synthesis using LPTEM a unique challenge that is possible when beam effects can be quantified and mitigated. With new direct sensing, high frame-rate cameras, and advances in liquid cell holder designs, combined with a growing understanding of irradiation effects and proper experimental controls, microscopists have been able to make strides in observing traditionally problematic carbon-based materials under conditions where synthesis can be controlled, and imaged free from beam effects, or with beam effects quantified and accounted for. These materials systems and LPTEM experimental techniques are discussed, focusing on nonradiolytic chemical and physical transformations relevant to materials synthesis.

Introduction

Synthetic carbon-based nanomaterials are a large and rapidly growing class of functional materials that have many potential advantages, which include biocompatibility, low cost of precursors, and the sheer structural and chemical diversity that is possible.[1–3] Indeed, there are myriad different structures that can be created using DNA and peptide structural programing, reticular building-block design, or control over assembly and crystallization.[3–6] However, these complex carbon-based nanostructures are often acutely sensitive to synthesis conditions, and the typical brute force method of materials development, trial and error testing of different synthesis conditions, is not feasible.[4,6,7] To accelerate materials development, having an understanding of the fundamental chemical and physical processes that underlie their synthesis will be critical, allowing a more systematic, informed approach to functional carbon material discovery.

While organic chemistry has developed tools for understanding chemical structure in a synthesis product or intermediate at a discrete period in time, including conventional transmission electron microscopy (TEM), methods for directly observing chemical, and morphological changes in solution over time, have long eluded researchers.[8–11] Most solution-phase (*in situ*) characterization methods rely on bulk scattering of some type of incident energy source—in carbon-based nanostructures, typically this would be light, x-rays, and neutrons.[12–15] While these indirect characterization methods can provide valuable information about the ensemble structure of the sample, some with high temporal resolution, the data from these scattering experiments require fitting to

Lucas R. Parent, Innovation Partnership Building, University of Connecticut, USA; lucas.parent@uconn.edu
Maria Vratsanos, Northwestern University, USA; mariavratsanos2023@u.northwestern.edu
Biao Jin, Pacific Northwest National Laboratory, USA; biao.jin@pnnl.gov
James J. De Yoreo, Pacific Northwest National Laboratory, and the University of Washington, USA; James.DeYoreo@pnnl.gov
Nathan C. Gianneschi, Northwestern University, USA; nathan.gianneschi@northwestern.edu
doi:10.1557/mrs.2020.224

models predicated on certain assumptions to interpret the raw data, and can be unreliable for exotic structures, polydisperse systems, or where *a priori* structural knowledge is lacking, as with novel materials.

While direct imaging electron scattering techniques (TEM and scanning electron microscopy [SEM]) have become common tools for material characterization, they have until recently been limited to samples in the solid phase—either dried or vitrified—making imaging or videoing solution phase dynamics inaccessible.[8,9] However, the development of liquid phase TEM (LPTEM) represents a facile way of observing solvated nanomaterials *in situ* and during synthesis.[16–18] In particular, LPTEM is becoming a powerful tool for carbon-based species as it provides significant advantages over indirect methods: no bulk averaging or model-fitting, and the ability to directly observe individual structures continuously over time.[19] LPTEM, as with any characterization method, has inherent limitations and artifacts that must be understood to conduct experiments that are not plagued by artefacts. TEM is a fundamentally destructive technique, and image contrast is reliant on the interaction between the incident irradiation (electron beam) and the sample.[20] Damage to the sample by the beam is exacerbated for solvated samples, as the solvent is additionally susceptible to radiolysis damage, which can propagate as secondary (chemical) damage to the solvated structures.[16] While these deleterious damaging effects may be mitigated using lower TEM fluxes, limiting the amount of energy transferred from the beam to the sample, they cannot be completely eliminated in a LPTEM experiment.

The last decade has seen several key technological developments in this area. New LPTEM sample holders and high-speed TEM cameras have in many ways made it possible to access LPTEM imaging conditions suitable for observing carbon-based nanomaterials in solution without significant beam damage—we point to several recent reviews specific to LPTEM holders and *in situ* TEM cameras.[19,21–24] However, finding LPTEM conditions where nonradiolytic synthesis processes can be observed in these systems is equally dependent on careful LPTEM experimental control by the microscopist, which is the focus of this article. We highlight LPTEM experimental practices that have proven successful, in three systems; biomolecules, biominerals, and organic reticular crystals.[73–76]

Biomolecules

Biomolecules represent an interesting class of material that broadly includes structures composed of nucleic acids, carbohydrates, amino acids, and lipids, as well as their respective derivatives. These compounds comprise the building blocks of the natural world and are able to natively assemble in physical materials with unparalleled precision via natural templating processes. This creates an interesting juxtaposition for this class of materials: while still amorphous, the defined, discrete structures of the constituents are evocative of the precision of crystalline materials. In fact, many biomolecules are able to assume crystalline phase structures. The innate functionality and precision of these biomolecular materials make them extremely attractive candidates for synthetic materials, wherein their native properties and amenability to sequence-programming could be harnessed for innumerable applications—peptide drugs, polysaccharide tissue scaffolds, and lipid membranes, to name a few. However, one of the major barriers to achieving synthetic control of biological materials is a lack of understanding of their basic formation processes; specifically, how and why their biomolecule building blocks assemble into different conformations. Biological matter, in general, has been challenging to study with electron microscopy.[25,26]

The Gianneschi group prepared a cyclic peptide with a defined cleavage site, which, when exposed to the appropriate enzyme, linearizes to stack as beta sheets, consequently forming fibrils that assemble to a gel structure.[27] To study the fibrilization and gelation processes *in situ* by LPTEM, the peptide and enzyme solutions were mixed and immediately placed between SiN_x window chips and loaded into the TEM, where they observed the transition from a structureless solution to one with many growing aggregates over time (**Figure 1**a). Critically, Touve and co-authors were able to confirm that the peptide building blocks that assembled into

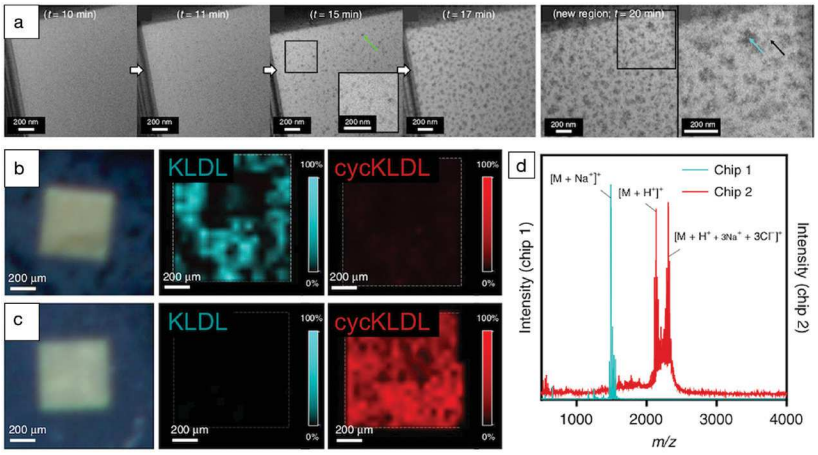

Figure 1. (a) Liquid phase transmission electron microscopy (LPTEM) time lapse of the evolution of aggregates from soluble peptide after tris(2-carboxyethyl)phosphine) (TCEP) reduction *in situ*.[27] (b–d) Confirmation of conserved (b) linear and (c) cyclic peptide molecular weight peaks via MALDI-IMS following the LPTEM experiment. (d) The presence of the unchanged molecular weight peak in the imaging window indicates that the sample material was not damaged by the imaging conditions. Note: KLDL, peptide sequence; MALDI-IMS, matrix-assisted laser desorption ionization imaging mass spectroscopy.

structure survived the LPTEM experiment undamaged using *postmortem* matrix-assisted laser desorption ionization imaging mass spectroscopy (MALDI-IMS) (Figure 1b–d). The peptide had a defined molecular weight and a known cleavage product, which was confirmed by the *postmortem* MALDI analysis, indicating that the observed structural transformations were solely due to the reaction with the enzyme tris (2-carboxyethyl)phosphine hydrochloride rather than a beam degradation process (Figure 1d). Complementary experiments were done at much greater fluxes and fluences as well, where the corresponding *postmortem* lacked the characteristic peptide peak indicating beam damage at those higher flux/fluence conditions. The authors created a damage plot for their sample, or an evaluation of "safe" imaging conditions, which can be similarly done for other systems studied by LPTEM.

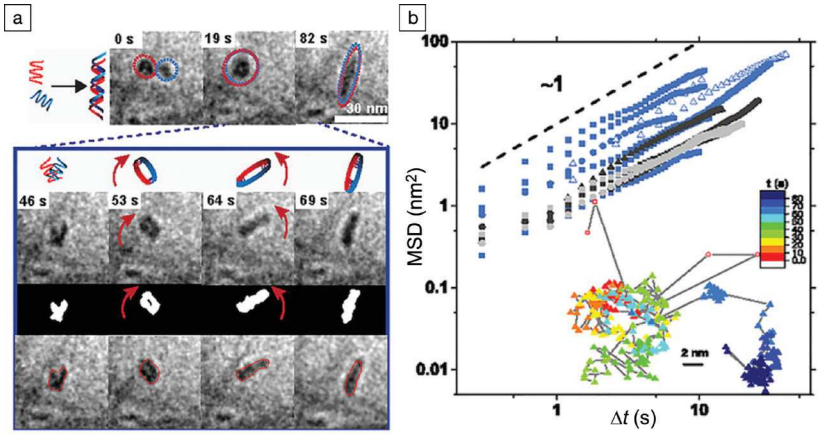

Figure 2. (a) Random sequence complementary single-stranded DNA hybridizing and rotating captured by liquid phase transmission electron microscopy. (b) Plots of mean square displacement (MSD) of structure centroids as a function of time. Inset (lower) shows projected motion in the *x*-*y* plane for sample from (a).[28]

The Granick group was also interested in observing biomolecule assembly, but at the level of individual DNA strands.[28] To study these processes, they designed 90 base-pair sequences of single-stranded DNA that they created as random, block, and hairpin sequences, which assemble (hybridize) with their complimentary molecules. Using *in situ* LPTEM and solutions of the different DNA, assembly and hybridization processes were observed in real time, which proceeded though the dimer-pair moving and rotating as a rigid, rod-like structure (**Figure 2**a), but with subtle variations specific to each DNA sample. Notably, the different random sequences selected would result in the same ultimate structure, but provided different metastable intermediate states, which are nearly impossible to characterize using traditional single molecule methods such as cryo-TEM or bulk x-ray scattering. Utilizing graphene liquid cells to encapsulate the DNA solution, hybridization of the engineered DNA strands was visible under low accelerating voltages (80 keV) and low flux conditions. Fickian motion of the assembled structures was also reported and observed to be independent of structure (Figure 2b). This displacement was linearly proportional to time, indicating to Wang and co-authors that motion was unhindered and that molecular structures were intact.[28] These experiments gave unprecedented insights into the transient states adopted by these structures whilst assembling, as well as intermediary steps used in error correction.

The Li group used *in situ* liquid phase scanning transmission electron microscopy (LPSTEM) to study the growth processes of hierarchical three-dimensional (3D) DNA structures (**Figure 3**).[29] Experimentally, long chain DNA structures created via rolling circle amplification (RCA), an isothermal amplification technique for nucleic acids that generates tandem repeats by adding single nucleotides to a circular template, were loaded into the liquid cell and inserted in the TEM. Because these RCA assemblies do not rely on Watson–Crick interactions and are thus sequent independent, the structures begin to amass spontaneously. They observed the initial long-chain DNA seeds subsequently grew and agglomerated into flower-like superstructures, confirming the hypothesized three-step assembly mechanism.[29] Watching this process in real time gives insights into the three-step kinetic formation process: spherical nucleation, crystal agglomeration and growth, and supramolecular formation of floral nanostructures. Knowledge of these superstructures may be formulated to allow superior size and morphological control.

Continuing in the vein of observing nucleation and growth processes of different biomolecules, the Tsukamoto

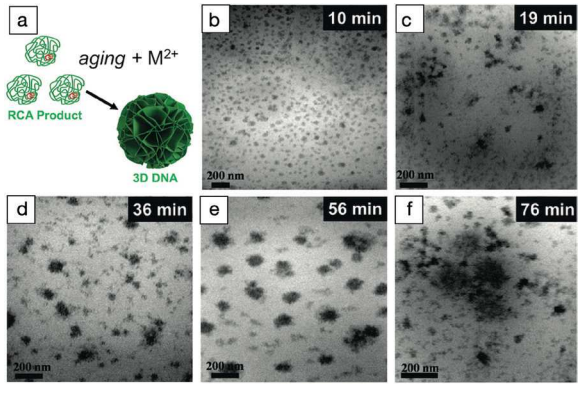

Figure 3. Liquid phase scanning transmission electron microscopy observation of the nanostructure assembly from functional nucleic acids; formation of spherical nuclei, growth and agglomeration of crystallites, and nanoflower assembly.[29]

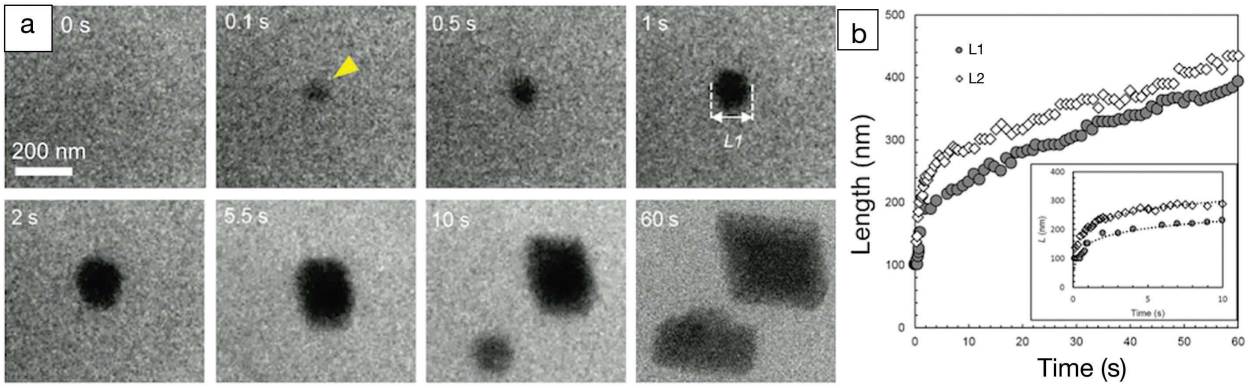

Figure 4. (a) Transformation of spherical nucleus L1 into an orthorhombic crystal observed by liquid phase transmission electron microscopy. Scale bar = 200 nm. (b) Dimensions of nucleated particles L1 and L2 over time, showing a slow to steady-state growth rate.[34]

group used LPTEM to confirm that the mesoscopic clusters that form the nuclei of protein crystals can be composed of amorphous solid particles (ASPs), rather than dense liquid as previously thought. These ASPs serve as heterogeneous nucleation sites.[30] In LPTEM, orthorhombic and tetragonal crystals were observed to form off of the ASPs with the latter dissolving in time, indicating that the former is the more stable polymorph (**Figure 4**a). Here, diffraction was used to indicate the presence of crystallinity in the observed particles. Flux dependence on sample damage and behavior was also investigated, and it was observed that at higher electron fluxes, protein crystals would dissolve. At more moderate dose rates, an initial spike in growth rate was measured, before the kinetics leveled off to the bulk rate after several seconds, indicating shifts in growth kinetics and mechanisms (Figure 4b). These observations are critical for mechanistic understanding of organic crystal formation, as the amorphous particles may serve either as precursors for crystal growth or heterogeneous nucleation sites.

Biominerals

Biomineralization comprises the set of processes by which organisms produce materials-based solutions to their functional requirements.[31] While these processes operate under biological control, they nonetheless reflect the physical and chemical principles that govern formation of inorganic minerals. The introduction of additives is a central feature of biomineral formation. These include inorganic ions, such as Mg, Sr, or phosphate, and organic molecules, such as proteins, polysaccharides, and metabolites, which serve either as insoluble matrices in which minerals form or as soluble constituents that modify mineral growth.[32–38] In the case of crystalline biominerals, key lines of inquiry thus seek to understand the pathways and dynamics of mineral nucleation and growth, as well as the means by which such additives affect these processes. Both require direct experimental evidence; thus LPTEM has become an important technique for understanding the crystallization of biomineral phases.[17] Studies have included formation of iron oxides in the presence of proteins associated with biological magnetite, mineralization of calcium phosphate in simulated body fluid, and nucleation and growth of calcium or cobalt carbonate ($CaCO_3$, $CoCO_3$) in either pure solution or in the presence of insoluble and soluble additives.[39–47] Here, we focus on carbonate mineral phases, as they constitute carbon-based materials.

$CaCO_3$ is among the most widespread of biomineral phases. Its deposition history reflects the interaction of Earth and biota since the Precambrian period, and $CaCO_3$ deposits comprise the largest terrestrial reservoir of CO_2 on the planet. Crystallization of $CaCO_3$ has been attributed both to classical monomer-by-monomer nucleation and growth processes and transformation of an initially formed amorphous $CaCO_3$ (ACC) phase.[48,49] To investigate these processes, LPTEM was applied over a wide range of supersaturations.[46] The results

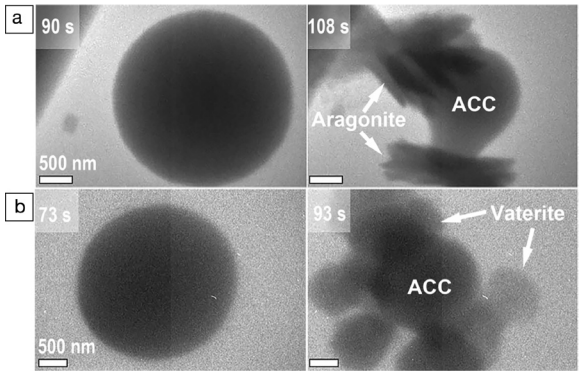

Figure 5. Liquid phase transmission electron microscopy investigations of $CaCO_3$ (ACC) formation and transformation. The direct transformation of amorphous ACC to (a) aragonite and (b) vaterite.[46]

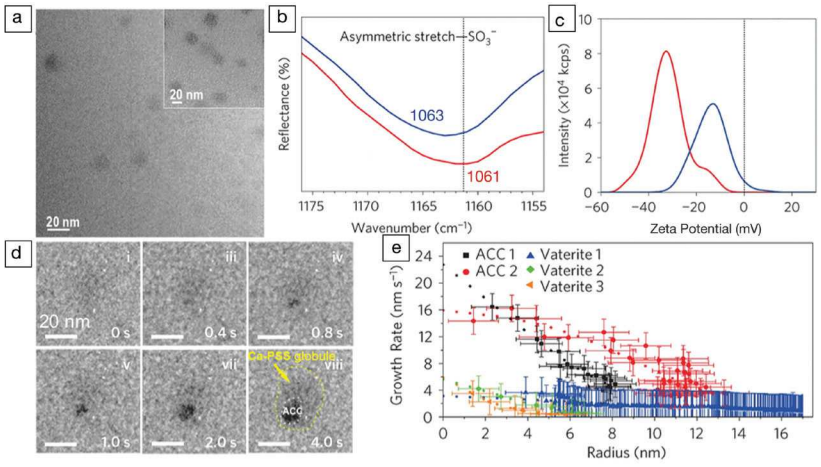

Figure 6. The formation of amorphous $CaCO_3$ (ACC) in the presence of poly(styrene sulphonate) (PSS). (a) Liquid phase transmission electron microscopy images of Ca-PSS globules. (b, c) fourier transform infrared spectroscopy spectrum (b) of the asymmetric stretch of the sulfonate group and zeta potential (c) for the Ca-PSS solution (blue) and the solution containing only PSS (red). (d) Initial nucleation and growth of ACC within the Ca-PSS globules. Scale bar = 20 nm. (e) Extrapolated growth rates versus average radius for two ACC particles (ACC 1 and 2 with PSS) compared against those of three vaterite particles (without PSS).[45]

revealed multiple nucleation pathways being operative simultaneously. When crystallization occurred via an ACC precursor, two pathways were observed. In the first, nucleation of the crystalline phase occurred independently and drove dissolution of the more soluble ACC. In the second, crystallization occurred through nucleation on or within the ACC particle to form aragonite (**Figure 5**a) and vaterite (Figure 5b) and a physical connection was maintained between the ACC particle and the growing crystal.

The previously mentioned study highlights the question of how the formation and transformation of ACC occurs. But it remains unclear how the transformation is controlled by the insoluble matrix. To address this question, poly(styrene sulfonate) (PSS), which is a negatively charged polyelectrolyte used to mimic the polysaccharides that control formation of certain marine biominerals,[37,38] was introduced into the $CaCl_2$ solution used in the nucleation experiments.[45] Supersaturation was established by flowing the Ca-PSS solution through one inlet and diffusing carbonate from a gaseous source through the second inlet. In the absence of PSS, direct nucleation and growth of vaterite on the silicon nitride substrate was the dominant outcome. When PSS was introduced, Ca-PSS globules were produced (**Figure 6**a), which contained over 50% of the Ca^{2+} due to complexation with the sulfate groups of the PSS, as evidenced by *in situ* Fourier transform infrared spectroscopy (FTIR) (Figure 6b) and zeta potential measurements (Figure 6c). Subsequently, the introduction of carbonate into the cell, drove formation of ACC nanoparticles exclusively within the globules (Figure 6d). The mineral remained amorphous for the duration of the experiment, except when left under the electron beam, which induced crystallization to calcite. Measurements of growth rates for ACC in the Ca-PSS globules and vaterite nanoparticles in the absence of PSS (Figure 6e) provided quantification of the supersaturation and showed that the supersaturation in the globules with respect to ACC was higher than in the PSS-free cell with respect to vaterite. Thus, the PSS plays three roles: It sequesters the Ca^{2+} so that no nucleation takes place outside of the globules; PSS suppresses formation of any crystalline phases so the supersaturation can build up to enable ACC formation; and it stabilizes the ACC. These findings demonstrate that ion binding can direct nucleation, providing insight into the potential role of acidic matrices in controlling biogenic ACC.

Living systems must control the shape of the mineral components. ACC, which is a moldable precursor, is thought to be critical to this process, thus the transformation of biogenic ACC into crystalline phases with complex shapes requires a source of regulation.[50] Common soluble additives associated with biominerals include Mg ions, carboxylated molecules and acidic proteins rich in aspartic or glutamic acid.[32,36,51] Poly(acrylic acid) (PAA) and citrate are often used

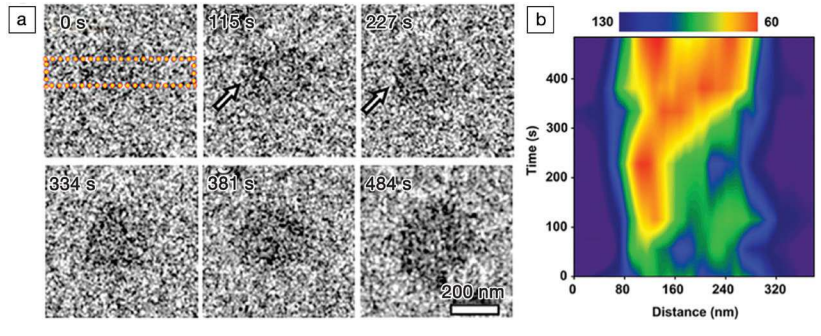

Figure 7. The phase transformation of amorphous $CaCO_3$ (ACC) to calcite by liquid phase transmission electron microscopy. (a) The direct solid-state transformation process of a single Mg-ACC particle to spherical Mg-calcite in the presence of 5.0 mM Mg^{2+}. (b) Change in the distribution of gray values of the particle in (a) with time, showing the spread of the area of high contrast throughout the particle.[41]

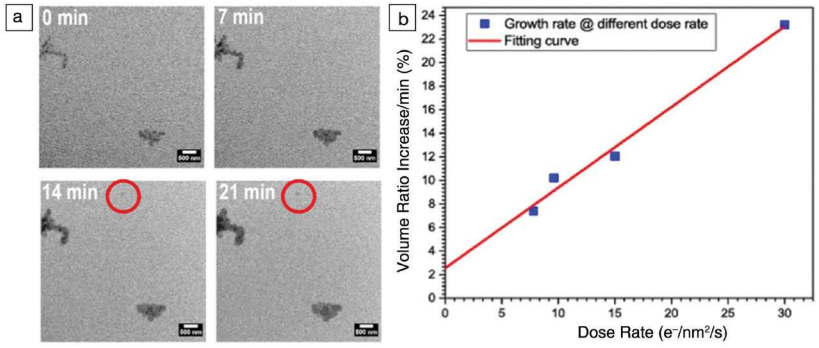

Figure 8. Liquid phase scanning transmission electron microscopy studies of $CoCO_3$ formation and growth. (a) Bright-field scanning transmission electron microscope images of $CoCO_3$ growth at an electron dose rate of 15.6 $e^-/nm^2/s$. The red circle marks nucleation of a new primary particle. (b) Linear dependence of the volumetric growth rate of amorphous $CoCO_3$ particles on electron dose rate.[42]

as surrogates to study the function of acidic macromolecules in biomineral formation.[52,53] These constituents have been implicated in stabilizing amorphous phases and controlling formation of crystalline phases, however, the mechanisms are poorly understood.

To explore these processes, the evolution of ACC to calcite in the presence of Mg^{2+}, sodium citrate (Na-Cit), and sodium poly-acrylate (PAA-Na) was visualized by LPTEM.[41] The results show that the transformation occurs via dissolution-reprecipitation for Na-Cit (0.5 mM), PAA-Na (250 µg/mL) and low concentrations of Mg^{2+} (≤2.5 mM), with additives either increasing ACC lifetimes (Mg^{2+}), retarding crystal formation/ACC dissolution (Na-Cit), or both (PAA-Na) (**Figure 7**a). However, introduction of Mg^{2+} at concentrations of ≥5.0 mM switches the ACC-to-calcite transition pathway from dissolution–reprecipitation to a shape-preserving direct transformation. Image contrast analysis during the transformation revealed a sharp change beginning at one location within the ACC nanoparticles and translating through the particles (Figure 7b). Phase analysis showed that the initially amorphous particles transformed to Mg-calcite. Moreover, *in situ* attenuated total reflection-FTIR spectroscopy and thermogravimetric analysis showed that the introduction of Mg^{2+} increases the amount of structural water in the ACC, while molecular dynamics predicted this increased water content destabilizes the ionic network thus enabling the solid-state rearrangement leading to the shape-preserving transformation. These findings suggest a rationale for the common presence of Mg in $CaCO_3$ biominerals and a simple mechanism for defining complex biomineral shapes.

LPTEM studies have contributed to the understanding of particle attachment as a common mechanism of crystal growth.[54,55] LPTEM observations of $CaCO_3$ solutions containing a $CaCO_3$-binding protein showed that particle growth can occur through amorphous particle attachment, in this case, of ACC onto calcite followed by its crystallization.[47] While the existence of a free solution phase in the biomineralizing environment is unlikely, many biominerals are known to form from aggregates of initially amorphous nanoparticles.[56] Recently, amorphous cobalt carbonate ($CoCO_3$) was also found by LP(S)TEM to also grow via particle attachment (**Figure 8**a).[42] Primary amorphous particles were found to nucleate and grow to ~10 nm before undergoing attachment to others. This conclusion was supported by cryo-TEM and dynamic light-scattering (DLS) data. However, because the growth rate of the primary particles was affected by the electron beam, which increased the local pH (Figure 8b) and thus the supersaturation, the inherent growth kinetics were obtained by measuring the growth rate over a range of electron doses and then extrapolating the growth rate to zero electron flux (Figure 8b). The findings of this study combined with those described above define a coherent body of work that provides unique insights into the mechanisms and dynamics of nucleation, growth, transformation, and aggregation of biomineral phases, as well as the effects of insoluble organic matrices and soluble additives on these processes.

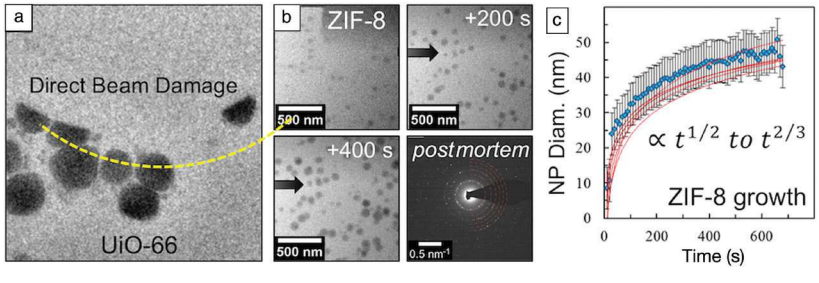

Figure 9. Liquid phase transmission electron microscopy (LPTEM) study of metal–organic framework (MOF) nanocrystal synthesis. (a) Direct etching damage of UiO-66 particles in water under e-beam at 300 keV. (b) LPTEM video time-lapse of undamaged ZIF-8 growth from methanol precursor solution at low flux (ca. 0.15 $e^-/Å^2s$). Lower right panel: *postmortem* diffraction pattern of MOFs formed during LPTEM experiment. (c) ZIF-8 growth curves extracted from the LPTEM videos for quantification.[57] Note: NP, nanoparticle.

Organic reticular crystals

Naturally occurring organic crystals with molecular-level periodicity (e.g., zeolites) have inspired the development of synthetic analogs, or reticular frameworks that use geometrically designed organic molecules/monomers as building blocks, either as purely organic

crystals or as hybrid metallic–organic crystals. The diversity of crystal structures and compositions that can be achieved using reticular synthesis is potentially limitless (infinite permutations of monomers and metal clusters), some of which express unparalleled materials properties.[4] However, scale-up of the synthesis of these materials remains a significant challenge.[7] LPTEM has the potential to accelerate materials development though fundamental studies into the underlying processes and pathways involved in reticular syntheses, and we highlight several recent examples.

Patterson et al. first reported the use of LPTEM to study reticular crystallization *in situ*, directly observing the growth of metal–organic framework (MOF) nanocrystals from premixed ligand/metal precursor solutions (**Figure 9**).[57] MOFs are composed of metal-cluster nodes linked by organic ligands, and are known to be highly susceptible to TEM beam damage in the form of loss of crystallinity (fluence threshold ca. 10–20 $e^-/Å^2$).[58,59] In LPTEM, solvated nanostructures also suffer (indirect) damage from secondary reactions with the irradiated solution, a steady-state concentration of radiolysis products.[60,61] The first objective was to establish LPTEM imaging conditions suitable to image premade MOF crystals in solution without damage. In water, Universitetet i Oslo MOF-66 (UiO-66) rapidly degraded by material etching at 300 keV (ca. 3 $e^-/Å^2s$) in a manner dominated by direct beam damage (Figure 9a), not by a solution radiolysis (chemical) effect. At 80 keV (same flux), where solution radiolysis is magnified, damage took the form of redeposition of material, attributed to the reaction of liberated ions from the damaged MOFs with the reductive radiolysis products of water to form (non-MOF) solid precipitates.[57,60] Zeolitic Imidazolate Framework-8 (ZIF-8), by comparison, was found to be sufficiently stable against both direct and indirect [chemical] beam damage at 300 keV and very low fluxes, ca. 0.15 $e^-/Å^2s$, when dispersed in methanol (Figure 9b). Methanol is known to form less reactive radiolysis products under irradiation (primarily: $H_2/H^•$, e^-_{solv}, and methoxyl radicals) than water, which can have the effect of reducing indirect (chemical) damage that might otherwise occur to the MOF in aqueous solution.[61–63]

With suitable experimental LPTEM conditions determined, the authors began their *in situ* study of the crystal growth.[57] A methanol-based ZIF-8 precursor solution was designed such that nucleation and grown of nanoparticles would occur on the minutes time scale at room temperature upon mixing the ligand and metal-salt precursor solutions, defined as $t = 0$. *In situ* LPTEM observation was started ca. $t = 5$ min after mixing the metal and ligand precursors, at which point, small MOF seed particles were dispersed over the entire liquid cell region (Figure 9b) that continued to grow individually over time without aggregation (or dissolution). Using multiparticle tracking algorithms and image analysis,[64] growth curves were extracted for each individual nanocrystal and for the ensemble of nanocrystals (Figure 9c), which indicate that (post-nucleation) ZIF-8 crystallization occurred via surface reaction-limited monomer addition (diameter $\propto t^{1/2}$ *to* $t^{2/3}$). *Postmortem* diffraction data (Figure 9b, bottom right) taken from the dried, disassembled chips confirmed that the growing particles were indeed the ZIF-8 crystal phase, validating the LPTEM growth data.[57]

Temperature is often a critical variable in the synthesis of reticular crystals. Smith et al. demonstrated the ability to incorporate variable temperature (VT) control into LPTEM experiments using a commercial holder and chips equipped with under-window heating elements.[65] The sample of interest was a purely organic crystal, or covalent organic framework (COF), composed of boronic acid-based monomers (COF-5) and synthesized in a complex organic solvent blend at elevated temperature.[66] COF-5 is a two-dimensional honeycomb crystal structure (sheets) that can grow as colloidal 3D molecular nanoparticles though inter-sheet pi-bonding.[67] For certain chemistry precursor mixtures,[68] colloidal COF-5 growth kinetics at room temperature can be so slow that a freshly mixed precursor solution has effectively no detectable nucleation/growth for hours until the point it is heated above ca. 55°C. In LPTEM at room temperature, the premixed COF-5 precursor solution, containing no preformed COF particles, was found to remain stable without detectable degradation or precipitation for many minutes under a continuous beam flux of ca. 0.25 $e^-/Å^2s$, indicating the monomers remained stable in the organic solvent at low continuous flux at 25°C.[65] However, upon heating the precursor solution to 90°C in hopes of triggering COF-5 nucleation, the resulting VT-LPTEM nanomaterial growth was drastically altered by beam effects due to the same continuous irradiation (**Figure 10**a). The structures were confirmed to be crystalline B_2O_3 particles, not COF-5, by *postmortem* TEM diffraction (Figure 10a, inset).[66]

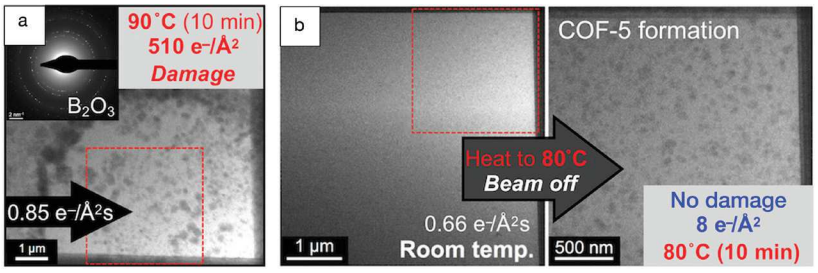

Figure 10. Variable temperature liquid phase transmission electron microscopy (VT-LPTEM) study of covalent organic framework (COF) nanocrystal nucleation and growth. (a) Magnified solution radiolysis and chemical damage when using VT-LPTEM at elevated temperatures; B_2O_3 crystals form from damaged COF-5 precursor under continuous low-flux irradiation at 90°C. (b) Low-fluence (and low-flux) stroboscopic VT-LPTEM of undamaged COF-5 nucleation and growth; $t = 0$ triggered by heating the precursor solution to 80°C; no damage to COF crystals for low cumulative fluence.[65]

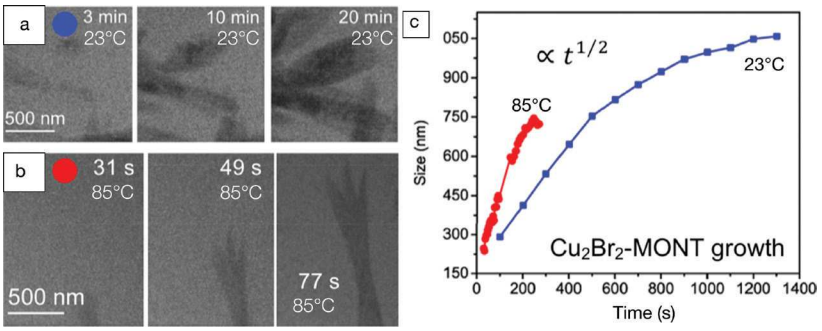

Figure 11. Low-flux (0.05 $e^-/Å^2s$) liquid phase transmission electron microscopy study of MONT crystallization at room temp and at 85°C. (a) Growth of Cu_2Br_2-metal–organic nanotube (MONT) nanocrystals at 23°C using stroboscopic imaging, and (b) at 85°C using continuous videography. (c) Growth curves for Cu_2Br_2-MONT crystallization at 23°C and 85°C.[71]

In radiolysis chemistry, increasing temperature has a magnifying effect on the yield and steady-state concentration of radicals/ions/e^-_{solv} in solution, as it accelerates rates of reactions in the physicochemical and chemical stages of molecule-radiolysis (to solution and crystals).[69,70] To overcome the additional beam damage when heating, the authors employed a low-flux, stroboscopic imaging technique to minimize the total fluence ($e^-/Å^2$) applied to the sample, where the beam was blanked between periodic images spaced over time (Figure 10b). Using this method for VT-LPTEM, individual COF-5 particles were observed to nucleate and grow by monomer addition without aggregation, ripening, or agglomeration when the solution was stabilized with acetonitrile, with particle growth arresting at ca. 20–30 nm diameter for the concentration studied. These VT-LPTEM data complemented results from bulk *in situ* scattering studies suggesting that acetonitrile functions to stabilize growing COF-5 seed crystals from inter-particle interactions that otherwise lead to aggregation and polycrystalline precipitation when acetonitrile is absent from the solvent mixture.[65]

Unfortunately, the stroboscopic LPTEM imaging technique necessarily reduces temporal resolution, which is less of a limitation for processes with appropriately slow kinetics. For organic reticular crystals generally, a cumulative fluence of ca. 10–20 $e^-/Å^2$ (at 200–300 keV) seems to be an upper limit of total tolerable irradiation, and this ultimately limits the frequency and number of frames that can be acquired in any experiment before beam effects start to manifest. Working with a Cu_2Br_2-based MOF system designed to crystallize as specific one-dimensional (1D) nanotubular morphologies, termed metal–organic nanotubes (MONTs), Vailonis et al. used a combination of *in situ* stroboscopic LPTEM at room temp (slow kinetics), and [continuous] videographic VT-LPTEM at 85°C (fast kinetics), both at low flux (ca. 0.05 $e^-/Å^2s$) and similar total fluence, to capture the underlying growth processes that occur at each temperature condition (**Figure 11**).[71] By monitoring the *in situ* growth of individual Cu_2Br_2-MONT crystals from a premixed precursor solution (Figure 11a–b), and extracting and analyzing their growth curves (Figure 11c), the authors found that at both room temperature and elevated temperature, tubular crystal growth was reaction limited (particle size $\propto t^{1/2}$), indicating that the formation of the 1D tubular morphology was driven by thermodynamic rather than kinetic effects at the solution concentration used. These *in situ* data provide evidence that the anisotropic growth that occurs during Cu_2Br_2-MONT crystal synthesis is due to the presence of thermodynamically preferred low energy surface sites, a fundamental insight which can inform future MONT materials development.[71]

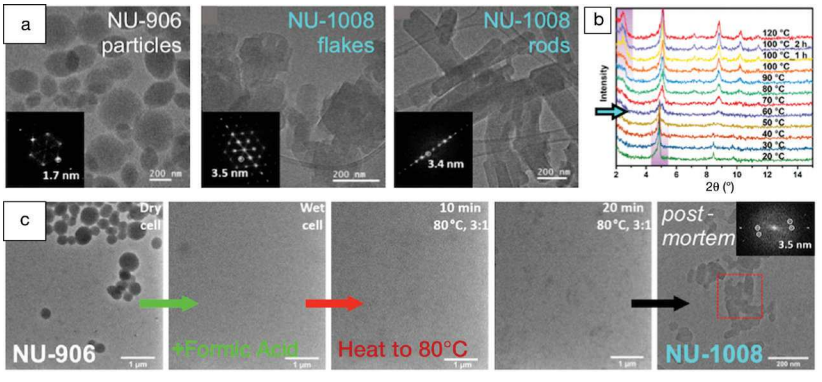

Figure 12. Studies of phase transition between polymorph crystal phases. (a) Dry-transmission electron microscope (TEM) time series of the transition of NU-906 particles into NU-1008 flakes that grow into NU-1008 rods. (b) *In situ* variable temperature (VT)-powder x-ray diffraction data of the phase transition in bulk solution, which largely occurs in the collection period indicated by the blue arrow. (c) VT-liquid phase (LP)TEM observation of the polymorph phase transition at 80°C that occurs through a multistep process; NU-1008 phase is confirmed by *postmortem* dry-TEM of the structures formed during VT-LPTEM (right panel).[72]

In a recent example of VT-LPTEM applied to MOF synthesis, Lyu et al. monitored the phase-transition process between polymorph phases in a Zr_6-based MOF system that can form multiple distinct crystal lattices depending on synthesis conditions, NU-1008 in formic acid or NU-906 in benzoic acid (**Figure 12**).[72] Preformed NU-906 particles can transform into NU-1008 particles when heated in formic acid, which can be used as a route to access diverse NU-1008 particle

morphologies or sizes. In bulk synthesis, pre-made spherical crystalline NU-906 particles transition into thin NU-1008 flakes after ca. 2 h in formic acid at 80°C, and then into large NU-1008 rods after 24 h by time-series dry-TEM and *in situ* powder x-ray diffraction (PXRD), which suggests some form of indirect transition between the 906 and 1008 phases (Figure 12a–b). Using VT-LPTEM and starting with preformed NU-906 particles that were then *in situ* solvated with formic acid (using inlet/outlet flow lines), the transformation process could be observed in time (Figure 12c), giving a clear view of the indirect transition, a multistep process involving the breaking down of the initial 906-crystal particles into units too small/low-contrast to be resolved in LPTEM (possibly individual monomers/metal-clusters or secondary building units, SBUs), and then reassembling the monomers/SBUs into new seeds that grow into individual NU-1008 crystal phase flakes and then rods from the available local solvated species.[72] This multistep process involving the complete disassembly of the starting NU-906 particles could not be resolved from the *in situ* variable temperature (VT)-PXRD data due to the bulk averaging effect that arises in PXRD data of ensembles of particles that all disassemble at slightly different starting times and with slightly differing disassembly rates, washing out the features that are due to the various individual transition steps (Figure 12b).

Summary and perspectives

Despite the ever-present challenges related to beam damage to carbon-based materials in TEM generally, experimental conditions and procedures have been found to effectively study these materials in solution. The recent LPTEM literature reviewed highlights some of the techniques that have enabled the observation of various chemical and physical transformations fundamental to the synthesis of carbon-based nanostructures. A key component has been the use of *postmortem* analysis, either structural (dry-TEM) or spectral (MALDI), to determine appropriate flux conditions and check for beam damage artefacts. However, there has yet to be a comprehensive beam-effects/damage study of carbon-based nanostructures using different solvents, concentrations, flux, fluence, and acc. voltage as variables beyond finding flux conditions where damage is sufficiently mitigated. Furthermore, there are still many basic questions regarding LPTEM experiments with these systems; how effective are different solvents or radiolysis scavengers at reducing damage? Is it purely the total cumulative fluence applied that determines damage threshold, or does rate (flux) also play a role (by how much)? Is there a flux threshold below which there is effectively no damage? What is the influence of the windows or confinement on nucleation and growth processes observed in LPTEM?

In practice, our LPTEM imaging capabilities, the quality of the data we acquire, are intimately tied to the microscope camera (imaging resolution/contrast and speed). The recent and continuing development of CMOS-based direct electron counting cameras has opened up new temporal and spatial resolutions in LPTEM experiments, but we stress that the best LPTEM raw data will only contain the minimum necessary signal (to reduce flux and extend observation time), and might look noisy to the naked eye. Instead of increasing flux/fluence to boost contrast or resolution of (low-Z) carbon structures, image/video postprocessing algorithms should be used, which can employ dynamic background correction, object thresholding, and object tracking, and can quantify kinetic processes captured in the data, such as nucleation event time-points or particle growth curves. Indeed, it is the ability to extract and quantify solution phase kinetics that makes LPTEM so potentially powerful for the study of chemical reactions and physical transformations. In the coming years, the development of robust multimodal *in situ* imaging and direct correlation between electron microscopy and scattering methods will be critical. The path toward structural and morphological elucidation of static dry state and cryogenic samples for soft and biological materials has been a long, but incredibly fruitful one. We look forward to the next decade of LPTEM developments as the field grows, becomes more competitive, and focuses its beam on dynamic chemical and physical transformations.

Acknowledgments

This manuscript was written with Government support under and awarded by the US Department of Defense through the ARO (W911NF-17–1-0326, W911NF-18–1-0359, and MURI W911NF-15–1-0568). In addition, N.C.G and L.R.P. thank the National Science Foundation (NSF) for support through Grant No. (CHE-1905270). M.V. thanks the NSF for support through the Graduate Research Fellowship Grant No. GRFP (DGE- 1842165). B.J. thanks the support from the US Department of Energy (DOE) Office of Basic Energy Sciences, Physical Sciences Division at Pacific Northwest National Laboratory (PNNL). PNNL is a multiprogram national laboratory operated for the DOE by Battelle under Contract No. DE-AC05–76RL01830.

References

1. P. Bhattacharya, D. Du, Y. Lin, *J. R. Soc. Interface* **11**, 20131067 (2014).
2. C. Cha, S.R. Shin, N. Annabi, M.R. Dokmeci, A. Khademhosseini, *ACS Nano* **7**, 2891 (2013).
3. L.P. Datta, S. Manchineella, T. Govindaraju, *Biomaterials* **230**, 119633 (2020).
4. Y. Cui, B. Li, H. He, W. Zhou, B. Chen, G. Qian, *Acc. Chem. Res.* **49**, 483 (2016).
5. A. Arakaki, K. Shimizu, M. Oda, T. Sakamoto, T. Nishimura, T. Kato, *Org. Biomol. Chem.* **13**, 974 (2015).
6. C.E. Callmann, M.P. Thompson, N.C. Gianneschi, *Acc. Chem. Res.* **53**, 400 (2020).
7. N. Stock, S. Biswas, *Chem. Rev.* **112**, 933 (2012).
8. E.G. Kelley, R.P. Murphy, J.E. Seppala, T.P. Smart, S.D. Hann, M.O. Sullivan, T.H. Epps, *Nat. Commun.* **5**, 3599 (2014).
9. J.P. Patterson, Y. Xu, M. Moradi, N.A.J.M. Sommerdijk, H. Friedrich, *Acc. Chem. Res.* **50**, 1495 (2017).
10. Y. Liu, G.J. Vancso, *Prog. Polym. Sci.* **104**, 101232 (2020).
11. L. Xiao, Z.D. Schultz, *Anal. Chem.* **90**, 440 (2018).
12. J.P. Patterson, M.P. Robin, C. Chassenieux, O. Colombani, R.K. O'Reilly, *Chem. Soc. Rev.* **43**, 2412 (2014).
13. D.A. Jacques, J. Trewhella, *Protein Sci.* **19**, 642 (2010).
14. J. Li, A. Jiao, S. Chen, Z. Wu, E. Xu, Z. Jin, *J. Mol. Struct.* **1165**, 391 (2018).
15. N.C. Santos, M.M. Domingues, *Front. Chem.* **6**, 237 (2018).
16. M.J. Williamson, R.M. Tromp, P.M. Vereecken, F.M. Ross, *Nat. Mater.* **2**, 532 (2003).

17. F.M. Ross, *Liquid Cell Electron Microscopy* (Cambridge University Press, Cambridge, UK, 2016).
18. L.R. Parent, E. Bakalis, M. Proetto, Y. Li, C. Park, F. Zerbetto, N.C. Gianneschi, *Acc. Chem. Res.* **51**, 3 (2018).
19. H. Wu, H. Friedrich, L.P. Patterson, N.A.J.M. Sommerdijk, N. de Jonge, *Adv. Mater.* 2001582 (2020), doi:10.1002/adma.202001582.
20. R.F. Egerton, P. Li, M. Malac, *Micron* **35**, 399 (2004).
21. M. Textor, N. de Jonge, *Nano Lett.* **18**, 3313 (2018).
22. N. de Jonge, L. Houben, R.E. Dunin-Borkowski, F.M. Ross, *Nat. Rev. Mater.* **4**, 61 (2019).
23. Q. Chen, C. Dwyer, G. Sheng, C. Zhu, X. Li, C. Zheng, Y. Zhu, *Adv. Mater.* **32**, 1907619 (2020).
24. A.R. Faruqi, G. Mcmullan, *Nucl. Instrum. Methods Phys. Res. A* **878**, 180 (2018).
25. W. Baumeister, *Ultramicroscopy* **9**, 151 (1982).
26. A. Engel, Y. Lyubchenko, D. Müller, *Trends Cell Biol.* **9**, 77 (1999).
27. M.A. Touve, A.S. Carlini, N.C. Gianneschi, *Nat. Commun.* **10**, 1 (2019).
28. H. Wang, B. Li, Y.J. Kim, O.H. Kwon, S. Granick, *Proc. Natl. Acad. Sci. U.S.A.* **117**, 1283 (2020).
29. M. Liu, Q. Zhang, B. Kannan, G.A. Botton, J. Yang, L. Soleymani, J.D. Brennan, Y. Li, *Angew. Chem. Int. Ed Engl.* **130**, 12620 (2018).
30. Y. Yamazaki, Y. Kimura, P.G. Vekilov, E. Furukawa, M. Shirai, H. Matsumoto, A.E.S. Van Driessche, K. Tsukamoto, *Proc. Natl. Acad. Sci. U.S.A.* **114**, 2154 (2017).
31. F. Nudelman, N.A.J.M. Sommerdijk, *Angew. Chem. Int. Ed. Engl.* **51**, 6582 (2012).
32. S. Bentov, J. Erez, *Geochem. Geophys. Geosyst.* **7**, 1 (2006).
33. M.J. Root, *Calcif. Tissue Int.* **47**, 112 (1990).
34. S. Bentov, S. Weil, L. Glazer, A. Sagi, A. Berman, *J. Struct. Biol.* **171**, 207 (2010).
35. Z. Zou, X. Yang, M. Albéric, T. Heil, Q. Wang, B. Pokroy, Y. Politi, L. Bertinetti, *Adv. Funct. Mater.* **30**, 2000003 (2020).
36. G. Fu, S. Valiyaveettil, B. Wopenka, D.E. Morse, *Biomacromolecules* **6**, 1289 (2005).
37. A.S. Schenk, I. Zlotnikov, B. Pokroy, N. Gierlinger, A. Masic, P. Zaslansky, A.N. Fitch, O. Paris, T.H. Metzger, H. Cölfen, *Adv. Funct. Mater.* **22**, 4668 (2012).
38. L. Addadi, J. Moradian, E. Shay, N.G. Maroudas, S.A. Weiner, *Proc. Natl. Acad. Sci. U.S.A.* **84**, 2732 (1987).
39. S. Kashyap, T. Woehl, X. Liu, S.K. Mallapragada, T. Prozorov, *ACS Nano* **8**, 9097 (2014).
40. X. Wang, J. Yang, C.M. Andrei, L. Soleymani, K. Grandfield, *Commun. Chem.* **1**, 1 (2018).
41. Z. Liu, Z. Zhang, Z. Wang, B. Jin, D. Li, J. Tao, R. Tang, J.J. De Yoreo, *Proc. Natl. Acad. Sci. U.S.A.* **117**, 3397 (2020).
42. H. Su, B.L. Mehdi, J.P. Patterson, N.A.J.M. Sommerdijk, N.D. Browning, H. Friedrich, *J. Phys. Chem. C* **123**, 25448 (2019).
43. R. Kröger, A. Verch, *Minerals* **8**, 21 (2018).
44. K.S. Dae, J.H. Chang, J.M. Yuk, J.Y. Lee, *Microsc. Microanal.* **23**, S1 (2017).
45. P.J.M. Smeets, K.R. Cho, R.G.E. Kempen, N.A.J.M. Sommerdijk, J.J. De Yoreo, *Nat. Mater.* **14**, 394 (2015).
46. M.H. Nielsen, S. Aloni, J.J. De Yoreo, *Science* **345**, 1158 (2014).
47. M.H. Nielsen, D. Li, H. Zhang, S. Aloni, T.Y.-J. Han, C. Frandsen, J. Seto, J.F. Banfield, H. Cölfen, J.J. De Yoreo, *Microsc. Microanal.* **20**, 425 (2014).
48. M. Jehannin, A. Rao, H. Cölfen, *J. Am. Chem. Soc.* **141**, 10120 (2019).
49. H.H. Teng, P.M. Dove, C.A. Orme, J.J. De Yoreo, *Science* **282**, 724 (1998).
50. B. Cantaert, D. Kuo, S. Matsumura, T. Nishimura, T. Sakamoto, T. Kato, *ChemPlusChem* **82**, 107 (2017).
51. D. Wang, A.F. Wallace, J.J. De Yoreo, P.M. Dove, *Proc. Natl. Acad. Sci. U.S.A.* **106**, 21511 (2009).
52. C. Shao, R. Zhao, S. Jiang, S. Yao, Z. Wu, B. Jin, Y. Yang, H. Pan, R. Tang, *Adv. Mater.* **30**, 1704876 (2018).
53. S. Matsumura, S. Kajiyama, T. Nishimura, T. Kato, *Small* **11**, 5127 (2015).
54. D. Li, M.H. Nielsen, J.R.I. Lee, C. Frandsen, J.F. Banfield, J.J. De Yoreo, *Science* **336**, 1014 (2012).
55. H. Zheng, R.K. Smith, Y.-W. Jun, C. Kisielowski, U. Dahmen, P. Alivisatos, *Science* **324**, 1309 (2009).
56. E.D. Eanes, J.D. Termine, M.U. Nylen, *Calcif. Tissue Res.* **12**, 143 (1973).
57. J.P. Patterson, P. Abellan, M.S. Denny, C. Park, N.D. Browning, S.M. Cohen, J.E. Evans, N.C. Gianneschi, *J. Am. Chem. Soc.* **137**, 7322 (2015).
58. Y. Zhu, J. Ciston, B. Zheng, X. Miao, C. Czarnik, Y. Pan, R. Sougrat, *Nat. Mater.* **16**, 53 (2017).
59. C. Wiktor, M. Meledina, S. Turner, O.I. Lebedev, R.A. Fischer, *J. Mater. Chem. A* **5**, 14969 (2017).
60. N.M. Schneider, M.M. Norton, B.J. Mendel, J.M. Grogan, F.M. Ross, H.H. Bau, *J. Phys. Chem. C* **118**, 22373 (2014).
61. T.J. Woehl, P. Abellan Baeza, *J. Microsc.* **265**, 135 (2017).
62. F.S. Dainton, G.A. Salmon, P. Wardman, *Proc. R. Soc. Lond. A Math. Phys. Sci.* **313**, 1 (1969).
63. J.H. Baxendale, P. Wardman, *The Radiolysis of Methanol: Product Yields, Rate Constants, and Spectroscopic Parameters of Intermediates*, National Standard Reference Data Series, National Bureau of Standards, **54** (1975).
64. C. Park, T.J. Woehl, J.E. Evans, N.D. Browning, *IEEE Trans. Pattern Anal. Mach. Intell.* **37**, 611 (2015).
65. B.J. Smith, L.R. Parent, A.C. Overholts, P.A. Beaucage, R.P. Bisbey, A.D. Chavez, N. Hwang, C. Park, A.M. Evans, N.C. Gianneschi, W.R. Dichtel, *ACS Cent. Sci.* **3**, 58 (2017).
66. B.J. Smith, W.R. Dichtel, *J. Am. Chem. Soc.* **136**, 8783 (2014).
67. A.M. Evans, L.R. Parent, N.C. Flanders, R.P. Bisbey, E. Vitaku, M.S. Kirschner, R.D. Schaller, L.X. Chen, N.C. Gianneschi, W.R. Dichtel, *Science* **361**, 52 (2018).
68. B.J. Smith, N. Hwang, A.D. Chavez, J.L. Novotney, W.R. Dichtel, *Chem. Commun.* **51**, 7532 (2015).
69. A.M. Evans, L.R. Parent, N.C. Flanders, R.P. Bisbey, E. Vitaku, M.S. Kirschner, R.D. Schaller, L.X. Chen, N.C. Gianneschi, W.R. Dichtel, *Science* **361**, 52 (2018).
70. M.A.H. De Penhoat, T. Goulet, Y. Frongillo, M.J. Fraser, P. Bernat, J.P. Jay-Gerin, *J. Phys. Chem. A* **104**, 11757 (2000).
71. K.M. Vailonis, K. Gnanasekaran, X.B. Powers, N.C. Gianneschi, D.M. Jenkins, *J. Am. Chem. Soc.* **141**, 10177 (2019).
72. J. Lyu, X. Gong, S. Lee, K. Gnanasekaran, X. Zhang, M.C. Wasson, X. Wang, P. Bai, X. Guo, N.C. Gianneschi, O.K. Farha, *J. Am. Chem. Soc.* **142**, 4609 (2020).
73. J.T. Early, K.G. Yager, T.P. Lodge, *ACS Macro Lett.* **9** (5), 756 (2020).
74. C. Li, C.C. Tho, D. Galaktionova, X. Chen, P. Král, U. Mirsaidov, *Nanoscale* **11** (5), 2299 (2019).
75. L.R. Parent, E. Bakalis, A. Ramirez-Hernandez, J.K. Kammeyer, C. Park, J. de Pablo, F. Zerbetto, J.P. Patterson, N.C. Gianneschi, *J. Am. Chem. Soc.* **139** (47), 17140 (2017).
76. A. Ianiro, H. Wu, M.M.J. van Rijt, M.P. Vena, A.D.A. Keizer, A.C.C. Esteves, R. Tuinier, H. Friedrich, N. Sommerdijk, J.P. Patterson, *Nat. Chem.* **11** (4), 320 (2019). □

Lucas Parent is a staff research scientist at the Innovation Partnership Building and the Center for Advanced Microscopy and Materials Analysis at the University of Connecticut. He received his BS degree in materials science from Rensselaer Polytechnic Institute in 2009, and his PhD degree in materials science from the University of California, Davis, in 2013. His research focuses on the development of *in situ* electron microscopy to study solution-phase formation, transition, and stimuli-response processes in carbon-based nanomaterials and biomaterials. Parent can be reached by email at lucas.parent@uconn.edu.

Maria Vratsanos is a doctoral candidate in materials science and engineering at Northwestern University. She received her undergraduate degree in polymer engineering with an emphasis on biomaterials at Case Western Reserve University in 2018. She is 2019 National Science Foundation Graduate Research Fellowship Program recipient. Her current research focuses on the investigation of soft-matter dynamics and transformations via liquid phase transmission electron microscopy. Vratsanos can be reached by email at mariavratsanos2023@u.northwestern.edu.

Biao Jin is a postdoctoral research associate at Pacific Northwest National Laboratory. He received his BE degree from Hainan University, China, in 2014, and his PhD degree in chemistry from Zhejiang University, China, in 2019. His current research focuses on nucleation and growth mechanisms of nanomaterials and *in situ* transmission electron microscopy techniques. Jin can be reached by email at biao.jin@pnnl.gov.

Nathan C. Gianneschi is the Jacob and Rosaline Cohn Professor of Chemistry, Materials Science and Engineering, Biomedical Engineering and Pharmacology at Northwestern University. He received his BSc degree from The University of Adelaide, Australia, in 1999, and his PhD degree from Northwestern University in 2005. He completed postdoctoral research at The Scripps Research Institute in 2008. He began his career at the University of California, San Diego. Gianneschi can be reached by email at nathan.gianneschi@northwestern.edu.

Jim De Yoreo is a chief scientist in materials science at the Physical and Computational Sciences Directorate at Pacific Northwest National Laboratory, and an affiliate professor of materials science and engineering and of chemistry at the University of Washington. He received his PhD degree in physics from Cornell University in 1985. His research focuses on interactions, assembly, and crystallization in inorganic, biomolecular, and biomineral systems. He served as president of the Materials Research Society (MRS) and is a Fellow of both MRS and the American Physical Society. De Yoreo can be reached by email at James.DeYoreo@pnnl.gov.